Macro- and Microspectroscopic Study of Nd (III) Uptake Mechanisms in Hardened Cement Paste

PETER MANDALIEV,*,†,‡,⊥ RAINER DÄHN,†
BERNHARD WEHRLI,‡,§ AND
ERICH WIELAND†

*Laboratory for Waste Management, Paul Scherrer Institute,
5232 Villigen PSI, Switzerland, Departement of Environmental
Sciences, Swiss Federal Institute of Technology (ETH),
8092 Zürich, Switzerland, and Swiss Federal Institute for
Environmental Science and Technology (EAWAG),
6047 Kastanienbaum, Switzerland*

Cement is an important component in repositories for low-level and intermediate-level radioactive waste. Nd uptake by hardened cement paste (HCP) has been investigated with the aim of developing a mechanistic understanding of the immobilization processes of trivalent lanthanides and actinides in HCP on the molecular level. Information on the microstructure of HCP, the Nd distribution in the cement matrix, and the coordination environment of Nd in these matrices was gained from the combined use of scanning electron microscopy (SEM), synchrotron-based μ-X-ray fluorescence (μ-XRF), μ-X-ray (μ-XAS), and bulk-X-ray absorption spectroscopy (bulk-XAS) on Nd doped cement samples. The samples were reacted over periods of time between 15 min and 200 days. SEM and μ-XRF investigations suggest preferential Nd accumulation in rims around "inner"-calcium silicate hydrates (C–S–H). The EXAFS data indicate that the coordination environment of Nd taken up by HCP was dependent on reaction time. Changes in the structural parameters derived from EXAFS support the idea of Nd incorporation into the structure of C–S–H phases. The Nd binding mechanisms proposed in this study have implication for an overall assessment of the safe disposal of trivalent actinides in cement-based repositories for radioactive waste.

Introduction

Cement-based materials play an important role in many multibarrier concepts developed worldwide for the safe disposal of radioactive wastes in deep geological repositories (*1*). The potential impact of radionuclides released from the near field of a repository can be controlled and reduced by a suitable choice of engineered and geological barriers. Knowledge of the long-term ability of the cement-based near field to retard the release of radionuclides into the far field and the chemical mechanism by which these radionuclides are bound to cement minerals are essential for safety analysis. Trivalent actinides such as $^{241/243}$Am are safety relevant radionuclides and therefore, a detailed understanding of the binding mechanisms of trivalent actinides in hardened cement paste (HCP) is essential for long-term assessments of the safe disposal of radioactive waste. At present, however, these mechanisms are only poorly understood at the molecular level.

In this study Nd(III) was regarded as a suitable chemical analogue for other lanthanides and trivalent actinides (e.g., Am(III), Cm(III)) as their ionic radii are comparable (*2*). HCP is a very heterogeneous material with discrete particles typically in the size range of about 2–200 μm, consisting of mainly calcium (aluminum) silicate hydrates (C–(A)–S–H), portlandite (calcium hydroxide), and calcium aluminates. Among the different cement phases, C–S–H phases are considered to be the most important constituent of HCP as they are abundant and expose a diversity of structural sites for cation and anion binding (e.g., (*3*)). In general it was observed that immobilization processes in cementitious systems are highly specific with regard to the mineral components and mechanisms involved (*4*).

The microspectroscopy study of Vespa et al. (*5*) showed a heterogeneous distribution of Ni in the Ni-doped compact cement matrix as well as Co accumulation in Ca-rich spots. Furthermore, it was shown that Ni(II) predominantly forms mixed Ni–Al layered double hydroxide phases and to a minor extent Ni(OH)$_2$. Only a few studies on the uptake of trivalent lanthanides and actinides, such as Nd(III), Eu(III), and Cm(III), by cementitious materials and C–S–H phases have been reported to date. Stumpf et al. (*6*) investigated the interaction of Cm(III) with HCP under highly alkaline conditions using time-resolved laser fluorescence spectroscopy (TRLFS). The spectroscopic studies indicated that Cm(III) uptake predominantly occurs in the C–S–H fraction of HCP after prolonged reaction time. Schlegel et al. (*7*) postulated that Eu(III) substitutes for Ca^{2+} in the Ca sheets and the interlayer of C–S–H phases based on extended X-ray absorption fine structure (EXAFS) spectroscopy data. The study further indicated possible precipitation of a Eu(III)-containing C–S–H-like phase (surface precipitate) in line with Eu(III) solubility limits determined from coprecipitation experiments. In a recent TRLFS study with Cm(III), three different species were distinguished upon Cm(III) binding to a C–S–H phase (C/S ratio = 1.07) aged for 119 days (*8*). Based on crystallochemical considerations using the defect 11 Å tobermorite structure as model the authors concluded that two Cm(III) species were bound in the structure of amorphous C–S–H by substituting for Ca^{2+} in the Ca sheets and in the interlayer. The third species detected in the study was attributed to the presence of Cm(OH)$_3$.

The aim of this study is to investigate Nd uptake by HCP on the macro- and microscale. We followed an approach developed earlier (*4, 9, 10*) in which scanning electron microscopy (SEM), μ-synchrotron X-ray fluorescence (μ-XRF), μ-X-ray absorption (μ-XAS), and bulk-X-ray absorption spectroscopy (bulk-XAS) were combined to determine the binding mechanisms of Ni and Co in cement pastes. The combined approach provided spatially resolved information on the elemental distribution in the compact cement matrix, which included areas of metal accumulation and their association with specific cement minerals, and on the speciation of the element of interest in selected regions of interest (ROI) of the cement matrix and in bulk material.

* Corresponding author phone: +41-56-56-310-5443; fax: +41-56-310-3565; e-mail: Peter.Mandaliev@psi.ch.
† Paul Scherrer Institute.
‡ Swiss Federal Institute of Technology (ETH).
§ Swiss Federal Institute for Environmental Science and Technology (EAWAG).
⊥ Present address: Laboratory for Solid State Chemistry and Catalysis, Swiss Federal Laboratories for Materials Testing and Research (EMPA), 8600 Dübendorf, Switzerland; Phone: +41-44-823-4340, Petar.Mandaliev@empa.ch.

Combining μ-XAS and bulk-XAS measurements allowed microscale information to be assessed in terms of the relevance for the bulk matrix. In this study Nd was used as absorber atom as the absorption of Fe (K-edge at 7112 eV), which is an important element in the cement matrix ($\sim$2.5 wt. % Fe in cement), does not interfere with the Nd L_{III}-edge (6208 eV) in spectroscopic measurements.

Materials and Methods

Cement Sample Preparation. Cement samples were prepared using a commercial sulfate-resisting Portland cement (CEM I 52.5 N HTS, Lafarge, France) and a procedure described in detail elsewhere (4). Briefly, metal-enriched hardened cement pastes were prepared by mixing a $Nd(NO_3)_2$ solution with unhydrated cement powder. The Nd stock solution (10^{-3} M) was prepared by dissolving the metal salt ($Nd(NO_3)_3 \cdot 6H_2O$, Merck "pro analysis") in deionized water and adding an aliquot HNO_3(conc.) for acidification. Aliquots of the acidified stock solution were mixed with the unhydrated cement powder at a water/cement (w/c) ratio of 0.4 according to a standard procedure (European Norm EN-196-3). The final metal concentration of the pastes was 26 μmol Nd/g HCP. The pastes were cast in Plexiglas molds, which were tightly closed with polyethylene snap caps, and aged up to 200 days. The cylindrical samples (diameter 4.1 cm, height 1 cm) were stored in closed containers at room temperature at 100% relative humidity in a glovebox under a N_2 atmosphere. Upon hydration, the samples were immersed in acetone for 24 h and dried in an oven at 40°. One portion of the HCP material was used for the preparation of polished thin sections (thickness $\leq$30 μm) for further use in the SEM-based analysis and synchrotron-based μ-XRF/XAS investigations. The other portion of the HCP material was crushed and sieved to obtain cement material (particle size <63 μm) for use in the bulk-XAS measurements.

Nd sorption samples for the bulk-XAS measurements were prepared according to a procedure described elsewhere (9). Briefly, 1 g of previously hydrated cement powder was mixed with 35 mL of artificial cement pore water (pH = 13.3). Details on the chemical composition are given elsewhere (11). Appropriate volumes of an acidified Nd stock solution (10^{-1} M) were added to the suspension to achieve final metal concentrations in the pastes of 26 μmol Nd/g HCP. After phase separation by centrifugation (60 min at 95,000g) the Nd treated cement samples were packed as a wet paste into Plexiglas sample holders and sealed with Kapton tape.

The list of samples including abbreviations, hydration time, and Nd metal loadings is given in Table S1 in the Supporting Information (SI).

Scanning Electron Microscopic Investigations. SEM analyses were conducted using a Zeiss DSM 962 microscope, operated at an accelerating voltage of 20 kV and a beam current of 76 μm. The microscope is equipped with a Si(Li)-detector for energy dispersive microanalysis (EDS). The spot size was $\sim$1 $\times$ 1 μm^2, and the penetration depth was $\sim$6 μm at the incident beam energy. The Zeiss DSM 962 microscope is equipped with a multiplier for backscattered electron (BSE) imaging and mineral phase specification, which is based upon differences in the gray scale.

μ-XRF, μ-XAS, and Bulk-XAS Data Collection and Reduction. μ-XRF maps were collected on the microXAS beamline at the Swiss Light Source (SLS), Switzerland, by scanning the samples under the monochromatic beam at the energy of 10000 eV (beam size $\sim$3 $\times$ 3 μm^2) and using a Si (111) crystal monochromator and a single element Si-detector. μ-XRF and μ-XAS Nd L_{III} edge data (6208 eV) were collected on beamline 10.3.2 at the Advanced Light Source (ALS), Berkeley, CA (12). The beamline 10.3.2 at the ALS is equipped with a Si (111) crystal monochromator. The monochromator angle was calibrated by assigning the energy

of 5989 eV to the first inflection point of the K-edge absorption spectrum of Cr metal foil. μ-XRF and μ-XAS measurements were collected at room temperature in fluorescence mode using a 7-element Ge solid state detector and a beam size of $\sim$5 $\times$ 5 μm^2.

Bulk-XAS spectra at the Nd L_{III} edge were collected on beamline BM26A (DUBBLE) at the European Synchrotron Radiation Facility (ESRF), Grenoble, France. The beamline is equipped with a Si (111) double-crystal monochromator. The monochromator angle was calibrated using a Cr metal foil. The measurements were conducted at room temperature in fluorescence mode using a 9-channel monolithic Ge solid state detector. For each sample, depending on the Nd loadings, between 3 and 7 spectra were collected to achieve the required signal-to-noise ratio.

The μ-XRF maps were processed using the Labview software package of beamline 10.3.2 (12) and MATLAB. Reduction and modeling of the XAS data was performed with the ATHENA/ARTEMIS package (13, 14). EXAFS data were dead-time corrected using the Labview software package of beamline 10.3.2 and with the internal detector acquisition electronic at the DUBBLE. Details of data reduction are given in the SI.

For the EXAFS analysis of Nd doped C–S–H phases, a model proposed earlier by Schlegel et al. (7) for Eu(III) retention by amorphous C–S–H phases with varying C/S ratios was used. In the present study Nd(III) uptake by C–S–H by substitution for Ca was assumed based on similarities in the ionic radii of the two elements (Nd^{3+}: 0.983 Å in 6-fold coordination; Ca^{2+}:1.00 Å and 1.07 Å for 6- and 7-fold coordination, respectively) (2). Statistical F-tests (15–17) were performed by testing various fit models and using the resulting crystallographic R-factors from the EXAFS fits to provide evidence for the best EXAFS fit model capable of reproducing the backscattering contributions from Si and Ca within the second shell at $R_{Nd-Ca/Si} \sim$ 3.6–4.0 Å. Details on the F-tests are shown in the SI. Based on the crystallographic data of nondoped tobermorite, which is considered to be a good model for the structure of poorly ordered amorphous C–S–H, and the results from the F-test, it was assumed that the proposed EXAFS model with backscattering contributions from Si and Ca in the given R range is suitable to reproduce the short-range order (<5 Å) in the structure of C–S–H phases.

Results and Discussion

Distribution of Nd in the Cement Matrix. Figure 1 shows a BSE image and elemental distribution maps of the Nd doped HCP sample aged for 200 days. BSE imaging allows identification of minerals of different compositions based on the gray scale contrast (18). The "inner"–C–S–H fills up the space originally occupied by the alite grains (Figure 1a). "Outer"–C–S–H (Figure 1a), which is less dense than "inner"–C–S–H and therefore has a darker gray tone, fills the porous space between the clinker minerals initially occupied with water. The latter minerals form when heating a mixture of limestone or clay to a temperature of $\sim$1450 °C during cement production. Clinker minerals start dissolving in contact with water.

The Nd distribution map displayed in Figure 1b shows that Nd is preferentially accumulated in regions with "inner"–C–S–H. The latter regions can be recognized from the Ca map (Figure 1c) as the fluorescence intensities show presence of clinker minerals. Metal accumulation around "inner"–C–S–H phases was previously observed in a Ni-doped HCP (4). The authors proposed that the clinker mineral alite, which dissolves faster than belite, forms highly reactive zones of "inner"–C–S–H phases. These zones may exhibit a high surface area, which promotes uptake and, consequently, facilitates metal accumulation in these areas.
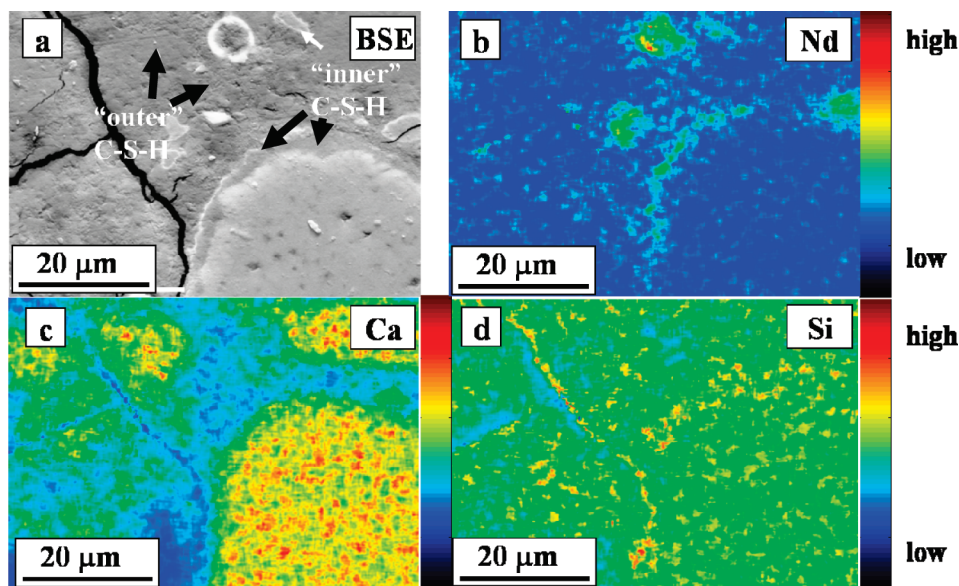
FIGURE 1. BSE image and elemental distribution maps of Nd, Ca, and Si in 60 × 50 μm overview of a Nd enriched hydrated cement matrix with a water/cement ratio of 0.4, a hydration time of 200 days, and a final metal concentration of 26 μmol Nd/g solid phase. The color bar represents relative Nd metal enrichments in the sample.
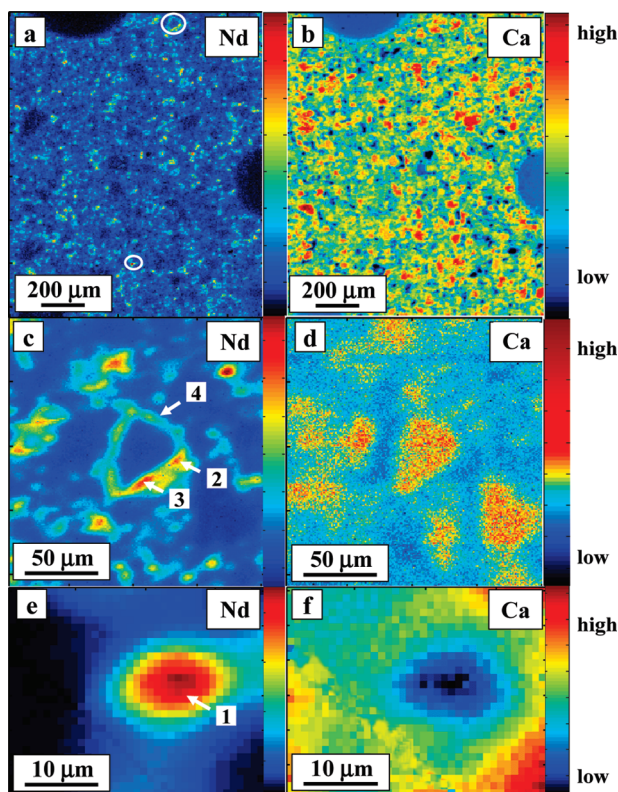

FIGURE 2. μ-XRF elemental distribution maps of Nd and Ca for the Nd doped HCP samples with a w/c ratio of 0.4, a hydration time of 28 days, and a final metal concentration of 26 μmol Nd/ g solid phase. Selected regions for μ-EXAFS measurement are labeled 1—4. The color bar represents relative metal enrichments in each sample.

The regions studied by SEM were also investigated by μ-XRF. Figures 2a and b show the elemental distributions of Nd and Ca in an overview map (~1400 μm × 1400 μm). The fine maps displayed in Figures 2c—f were collected in the areas encircled in Figure 2a. All μ-XRF maps supported the heterogeneous distribution of Nd and Ca in the cement matrix as previously observed with SEM-EDS. In particular, Nd accumulation in the rims around clinker minerals was

confirmed (Figure 1c). The μ-XRF maps also show Nd "spot-like" features in addition to rims. Note, that the vertical extension of the probed volume by μ-XRF is controlled by two factors: the penetration depths of the primary beam and the escape depth of the generated X-ray fluorescence. The latter is a function of the absorption length of the matrix, which, in turn, depends on the energy of the X-ray fluorescence and the electron density of the matrix. For Nd doped cement a penetration depth of ~56 μm was calculated based on typical cement composition and density. The latter penetration depth is larger than the sample thickness (≤30 μm). Therefore, the presence of Nd "spot-like" features in addition to rims could be attributed to the higher penetration depth of the synchrotron beam compared to SEM-EDS as reported elsewhere (4).

The μ-XRF maps further suggest anticorrelation between Nd and Ca in the different regions (SI). The speciation of Nd was determined on several ROIs using μ-EXAFS spectroscopy.

Speciation of Nd on the Microscale. Figure 3 shows (a) k^3-weighted, normalized, background subtracted μ-EXAFS spectra, (b) the corresponding radial structure functions (RSFs), and (c) k^3-weighted μ-EXAFS function for the Fourier-backtransform spectra of ROIs 1—4 in the CEMHYD-28-26 sample (Figure 2c, d) and ROIs 1—3 in the CEMHYD-200-26 cement sample (map not shown). The μ-EXAFS data are reported together with the corresponding bulk-EXAFS data. Additional μ-EXAFS spectra collected in ROIs 5—8 of the CEMHYD-200-26 sample are given in Figure S2.

The RSFs of all Nd doped HCP samples showed a peak at $R + \Delta R = 2.0$ Å, which was fit by assuming the presence of a single oxygen shell. The number (N) of neighboring oxygen atoms and the estimated Nd—O distances for all Nd doped HCP samples were found to be similar within the experimental uncertainties, e.g., $N_O = 7.1$ (±1.1) to 8.5 (±1.7) and $R_{Nd-O} = 2.44$ (±0.015) to 2.46 Å (±0.007) (Table 1). The Debye—Waller factor (DW) ranged in value between 0.006 (±0.001) Å^2 and 0.013 (±0.001) Å^2 in most cases.

Presence of further backscattering atoms was indicated by the broad peak in the Fourier transforms (FTs) at $R + \Delta R$ ~3.0 Å. This peak was fit by considering Nd—Si and Nd—Ca backscattering paths (SI). The μ-EXAFS measurements revealed variations in the EXAFS parameters of the neighboring Si and Ca atoms, which were determined on the different ROIs in the CEMHYD-28-26 sample. For example,
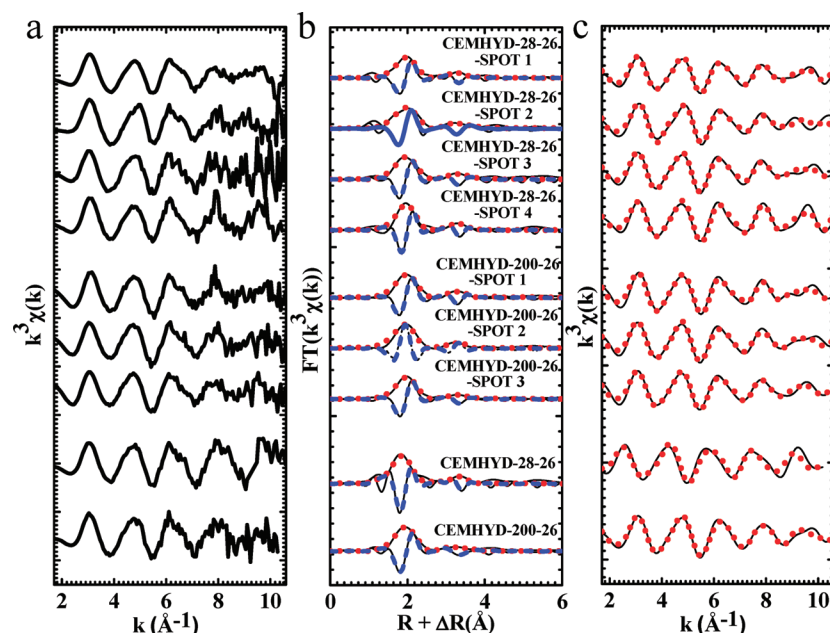
FIGURE 3. Selected Nd L$_{III}$-μ-EXAFS and bulk-EXAFS measurements for the Nd doped HCP samples with a w/c ratio of 0.4, varying reaction time only (15 min., 1 day and 200 days), and total metal concentrations of 26 μmol/g solid phase: (a) k^3-weighted spectra; (b) the corresponding RSFs of experimental (solid line) and fitted (dashed and dotted lines for the imaginary and the real part, respectively); (c) k^3-weighted EXAFS function for the Fourier-back-transform spectra obtained from Figure 3b (range: $R + \Delta R = 1.7-4.0$).

TABLE 1. Structural Information Obtained from Selected μ-EXAFS Nd L$_{III}$-Edge Data Analysis of Nd Doped HCP Samples^a (Spots 1–4 of the CEMHYD-28-26 Sample Are Indicated in Figure 2)

sample	ROI	$N_O{}^b$	$R_{Nd-O}{}^c$(Å)	σ^2 ^{d}>(Å^2)	$N_{Si}{}^b$	$R_{Nd-Si}{}^c$ (Å)	σ^2 ^{d}(Å^2)	$N_{Ca}{}^b$	$R_{Nd-Ca}{}^c$(Å)	σ^2 ^{d}(Å^2)	$\Delta E_0{}^e$ (eV)	$R_f{}^f$
	1	7.4 (1.3)	2.45 (0.011)	0.008 (0.001)	4.3 (0.7)	3.84 (0.04)	0.005	3.1 (0.7)	3.86 (0.05)	0.005	6.7 (1.1)	0.02
	2	8.2 (1.4)	2.45 (0.012)	0.013 (0.002)	5.1 (1.1)	3.78 (0.03)	0.003	4.7 (1.3)	3.84 (0.03)	0.005	7.3 (1.2)	0.03
	3	8.5 (1.7)	2.44 (0.015)	0.010 (0.002)	4.8 (1.4)	3.82 (0.03)	0.004	4.5 (0.8)	3.89 (0.03)	0.005	7.4 (0.9)	0.05
	4	7.1 (1.1)	2.45 (0.010)	0.006 (0.001)	4.6 (0.9)	3.84 (0.05)	0.004	2.4 (0.7)	3.88 (0.06)	0.005	8.1 (1.3)	0.06
CEMHYD-28-26	5	7.3 (1.3)	2.44 (0.011)	0.009 (0.002)	3.1 (0.7)	3.79 (0.03)	0.004	4.3 (0.9)	3.84 (0.03)	0.010	7.4 (1.4)	0.03
	6	7.7 (1.4)	2.45 (0.013)	0.013 (0.001)	3.4 (0.9)	3.81 (0.02)	0.004	3.1 (0.6)	3.87 (0.04)	0.005	7.3 (1.1)	0.07
	7	7.8 (1.1)	2.44 (0.012)	0.011 (0.001)	4.4 (1.4)	3.82 (0.04)	0.006	2.4 (0.6)	3.86 (0.02)	0.005	6.5 (0.7)	0.04
	8	7.2 (1.4)	2.46 (0.010)	0.010 (0.002)	3.7 (1.1)	3.85 (0.04)	0.005	2.9 (0.7)	3.85 (0.05)	0.010	7.6 (0.9)	0.04
	9	8.3 (1.6)	2.45 (0.008)	0.013 (0.001)	4.8 (1.3)	3.78 (0.04)	0.003	4.4 (1.1)	3.84 (0.04)	0.005	7.3 (1.2)	0.05
	1	8.1 (1.8)	2.46 (0.007)	0.010 (0.001)	6.4 (1.2)	3.87 (0.03)	0.004	5.5 (1.1)	3.93 (0.03)	0.005	6.1 (0.8)	0.03
CEMHYD-200-26	2	7.5 (1.1)	2.45 (0.010)	0.011 (0.002)	6.1 (1.5)	3.85 (0.02)	0.003	4.7 (1.3)	3.92 (0.02)	0.004	7.4 (1.1)	0.04
	3	8.4 (1.6)	2.45 (0.014)	0.012 (0.001)	4.9 (1.1)	3.86 (0.04)	0.003	5.7 (1.4)	3.93 (0.04)	0.004	7.3 (1.4)	0.02

^{a} Fourier-transformed $\chi(k)$ range $\Delta k = 1.7-10.3$ Å^{-1}. ^{b} Number of neighbor atoms. ^{c} Interatomic distance. ^{d} Debye–Waller factor. ^{e} Energy shift of the theoretical calculated spectrum to the energy grid of the measured spectrum. ^{f} The crystallographic R-factor.

the coordination number of Si varied between $N_{Si} = 3.1$ (±0.7) and 5.1 (±1.1) and the Nd–Si distances ranged from R_{Nd-Si} = 3.78 (±0.03) Å to 3.85 (±0.04) Å. The variations in the μ-EXAFS parameters of the neighboring Ca atoms were similar: $N_{Ca} = 2.4$ (±0.7) to 4.7 (±1.3) and $R_{Nd-Ca} = 3.84$ (±0.03) Å to 3.89 (±0.03) Å. The above findings reflect variability of the local coordination environment of Nd, which could be attributed to structural disorder in hydrating cement. Interestingly, the coordination numbers N_{Si} and N_{Ca} were significantly larger than those expected for Nd sorbed on solid phases. For example, for Nd sorbed onto portlandite, which is one of the main secondary phases forming in hydrating cement, lower N_{Ca} ($N_{Ca} = 2.1 \pm 0.8$) and shorter Nd–Ca distance were observed (3.66 $\pm$ 0.04 Å) (Table 2). Note that this finding agrees with results from an earlier study on Am(III) sorption onto ferrihydrite where one neighboring Fe was detected in the case of Am(III) inner sphere surface complexation (19). The structural parameters listed in Table 1 showed that the number of neighboring second shell atoms in all samples is >2, thus indicating structural incorporation of Nd into solid phases.

In contrast to the CEMHYD-28-26 sample, the μ-EXAFS parameters determined on three ROIs in the CEMHYD-200-26 sample were similar in value. Although the number of spots probed is limited, the data were remarkably consistent. For example, the coordination numbers of neighboring Si and Ca atoms ranged in value between $N_{Si} = 4.9$ (±1.1) to 6.4 (±1.2) and $N_{Ca} = 4.7$ (±1.3) to 5.7 (±1.4) (Table 1), respectively. These variations were smaller than in the CEMHYD-28-26 sample. Importantly, the average Nd–Ca distances were consistently longer than in the CEMHYD-28-26 sample (Table 1). The latter showed that Nd–Ca distances in the Nd doped HCP samples tend to become longer with increasing reaction time, thus suggesting incorporation into the Ca sheets of C–S–H. Note that about 5 next neighboring Ca atoms could be expected if Nd is bound into the Ca sheets, irrespectively of the calcium-to-silicon (C/S) ratio (20). Therefore, the number of next nearest Ca

sample (bulk-EXAFS)	N_O[b]	R_{Nd-O}[c] (Å)	σ^2 [d] (Å^2)	N_{Si}[b]	R_{Nd-Si}[c] (Å)	σ^2 [d] (Å^2)	N_{Ca}[b]	R_{Nd-Ca}[c] (Å)	σ^2 [d] (Å^2)	ΔE_0[e] (eV)	R_f[f]
CEMHYD-15 min-26	7.4 (1.5)	2.45 (0.014)	0.011 (0.001)	3.4 (0.8)	3.77 (0.05)	0.004	4.2 (0.9)	3.83 (0.04)	0.009	5.4 (0.8)	0.05
CEMHYD-1-26	8.3 (1.6)	2.46 (0.011)	0.010 (0.002)	4.4 (1.1)	3.79 (0.04)	0.003	4.4 (1.2)	3.86 (0.03)	0.004	6.5 (1.1)	0.03
CEMHYD-28-26	7.2 (1.2)	2.45 (0.010)	0.010 (0.001)	4.9 (1.0)	3.84 (0.03)	0.010	4.7 (1.1)	3.89 (0.04)	0.007	7.1 (1.4)	0.04
CEMHYD-200-26	8.5 (1.4)	2.44 (0.011)	0.011 (0.003)	6.5 (1.7)	3.88 (0.04)	0.004	5.1 (1.1)	3.93 (0.03)	0.003	7.2 (1.2)	0.03
CEMSORB-1-26	7.2 (1.4)	2.46 (0.013)	0.011 (0.002)	2.2 (0.5)	3.78 (0.03)	0.003	2.7 (0.7)	3.82 (0.04)	0.009	6.8 (0.9)	0.02
CEMSORB-28−26	6.7 (0.9)	2.46 (0.012)	0.010 (0.001)	2.8 (0.7)	3.79 (0.04)	0.003	3.9 (0.9)	3.83 (0.02)	0.009	7.1 (1.3)	0.04
CH-1-26 (Portlandite)	7.4 (1.1)	2.43 (0.012)	0.007 (0.002)	—	—	—	2.1 (0.8)	3.66 (0.04)	0.007	5.3 (0.8)	0.06

[a] Footnotes b–f are the same as those for Table 1.

atoms was considered to be a reliable indicator for Nd incorporation into C−S−H phases.

Speciation of Nd on the Macro-Scale. Bulk-EXAFS measurements allowed variability in the structural parameters on the microscale to be assessed with respect to their relevance for the bulk material. A comparison of the structural parameters listed in Table 1 with those listed in Table 2 allowed the two sets of corresponding structural parameters to be compared for the CEMHYD-28-26 and CEMHYD-200-26 samples. The data did not show significant differences in the structural parameters for the oxygen and the Si shells. However, differences were observed for Ca coordination numbers, N_{Ca}, in the short term samples ($\leq$28 days). For example, in CEMHYD-28-26, the bulk-EXAFS data indicated high coordination numbers ($N = 4.7 \pm 1.1$), while significantly lower coordination numbers ($N = 2.4 \pm 0.7$ to 3.1 ± 0.6 in ROIs 4, 6, 7, and 8) were observed on the microscale. The above finding suggests that coordination environments with lower Ca coordination numbers were not representative for the Nd doped material aged for short time periods. In contrast, the structural parameters determined from microspectroscopy and bulk-EXAFS measurements for the CEMHYD-200-26 sample agree very well, indicating that microscale variability in the local coordination environment of Nd in HCP was significantly reduced with increasing hydration time.

The bulk-EXAFS data listed in Table 2 further indicate changes in the Nd−Si and Nd−Ca bond distances with time. In the Nd doped samples aged for 15 min and 1 day (CEMHYD-15M-26, CEMHYD-1-26), the Nd−Si and Nd−Ca distances were determined to be $R_{Nd-Si} = 3.77$ (± 0.05) to 3.79 (± 0.04) Å and $R_{Nd-Ca} = 3.83$ (± 0.04) to 3.86 (± 0.03) Å. These distances compare well with those determined on few ROIs in the CEMHYD-28-26 sample. Nevertheless, the distances are shorter than those determined on the sample aged for 200 days (Table 2). This finding corroborates the trend toward longer Nd−Si and Nd−Ca distances with time, which was already indicated from the microspectroscopic data. Changes in the structural parameters with time reveal that the initial coordination environment of Nd determined after reaction times $\leq$1 day possibly represents a "metastable" configuration.

A Mechanistic Interpretation of Nd Immobilization in HCP. Exposing unhydrated cement to water generates a chemically very reactive system. A detailed description of the hydration process of cement CEM I 52.5 HTS and the corresponding thermodynamic modeling are given elsewhere (21). The hydration process starts in contact with water. In the first stage easily soluble solids such as the alkali sulphates and free lime dissolve, releasing Ca, Na, K, SO_4^{2-}, and OH^- into solution. Less soluble solids such as gypsum ($CaSO_4 \cdot 2H_2O$) and calcite dissolve partially until equilibrium conditions have been reached. In addition, the clinker phases (alite: Ca_3SiO_5; belite: Ca_2SiO_4; aluminate: $Ca_3Al_2O_6$; alumino-ferrite ($Ca_4(Fe_{x-1}Al_x)_4O_{10}$ solid solution)) slowly dissolve and continuously release Ca, Si, Al, Fe(III), and OH^- to the solution. In the early stage of cement hydration (<12 h) mainly portlandite, ettringite, and C−S−H phases precipitate. In this period oversaturation with respect to these secondary

minerals occurs (22). After 24 h, further evolution of the cement composition is controlled by the continuous formation of C−S−H phases and portlandite while the formation of ettringite is exhausted and formation of hydrotalcite and calcium monocarbonate starts (21). The final stage of cement hydration extends over years and is driven by slow dissolution of the clinker minerals alite and belite. In this stage the solution has a pH of about 13.3 (Na and K solution concentrations as the main counterions), while the solution concentrations of Ca and S are significantly lower than in the early stage, i.e., $\leq$ 24 h (Ca ~2 mM; SO_4^{2-} ~2 mM). The speciation of Nd in hydrating cement paste can be assessed with a perspective on the chemical conditions of the reacting cementitious system.

Upon adding Nd to the reacting cementitious systems several Nd species may appear: Nd bound on the surface of clinker and secondary minerals (outer- and inner-sphere surface complexes), Nd coprecipitated in solids with fixed and variable (solid solution) stoichiometries, and Nd incorporated in the structure of secondary minerals. Further, based on thermodynamic calculations, the formation of hydroxides (e.g., $Nd(OH)_3$(am)) was anticipated under the highly alkaline conditions of a cementitious system. Neither micro- nor bulk-EXAFS spectra showed the corresponding Nd−Nd scattering contributions, which allowed formation of $Nd(OH)_3$(am) in these systems to be excluded. Rapid formation of a mixed Nd−Ca precipitate, however, cannot be ruled out with a view to similarities in the EXAFS parameters of the CEMHYD-15M-26 and CEMHYD-1-26 samples analyzed in this study with those of a mixed Nd/Ca precipitate (23). The following structural parameters were determined for the precipitate: $R_{Nd-Si} = 3.81$ Å and $R_{Nd-Ca} = 3.84$ Å; $N_{Si} \sim 4.6$ and $N_{Ca} \sim 5.5$. Note that the latter coordination numbers and bond-distances are comparable to those in CEMHYD-15M-26, CEMHYD-1-26, and CEMSORB-28-26 (Table 2). Nevertheless, the lower N_{Ca} and N_{Si} coordination numbers observed in the CEMSORB-1-26 sample indicate formation of Nd surface complexes rather than Nd sorption and that only a small fraction of Nd is incorporated within the 28 days reaction time of sorption samples.

The structural parameter determined for the aged CEM-200-26 samples can be compared with those determined earlier on Nd doped, hydrothermally synthesized tobermorite (23). Note that tobermorite is considered to be an adequate model compound for the C−S−H phases forming in hydrating cement. The total inventory of Nd was found to be incorporated in the structure of the hydrothermally synthesized tobermorite (23). In the latter phase Nd has ~ 5 Si and ~ 6.7 Ca neighboring atoms at $R_{Nd-Si} = 3.87$ Å and $R_{Nd-Ca} = 3.91$ Å, respectively. This finding shows that Nd−Si and Nd−Ca bond distances tend to be longer in well-ordered crystalline C−S−H phases than in the Nd/Ca precipitate and Nd surface complexes. Furthermore, Nd was found to preferentially replace Ca in the Ca sheets of 11 Å tobermorite (23). The above bond distances agree very well with those determined for Nd in the CEMHYD-200-26 samples (Table 2), indicating Nd incorporation into the structure of C−S−H phases in hydrating cement. Nd−Ca substitution in the Ca

sheets of C–S–H phases is due to similarities in the ionic radii of the two elements in 6-fold coordination (0.983 and 1.00 Å, respectively). In the ideal tobermorite structure Ca from the central Ca sheet is surrounded by ~7 oxygens (R_{Ca-O} = 2.46 Å), 3–4 Si (R_{Ca-Si} = 3.67–3.73 Å) and about 5 Ca (R_{Ca-Ca} = 3.80–3.96 Å) (24). Therefore, our observation of about 5 nearest neighboring Ca atoms at $R_{Nd-Ca} \sim$ 3.87–3.91 Å suggests that, in fact, Nd is bound in the Ca sheets of the C–S–H phases present in HCP. H^+ or OH^-, respectively, could account for charge compensation (23).

EXAFS investigations of the Nd uptake by amorphous C–S–H phases further corroborate the finding of longer Nd–Si and Nd–Ca distances upon aging Nd doped C–S–H phases for up to 270 days (20). In particular it was observed that in the samples with the highest calcium-to-silica (C/S) ratio (C/S = 1.54) Nd–Si and Nd–Ca distances increased from about R_{Nd-Si} = 3.72 ± 0.04 Å and R_{Nd-Ca} = 3.77 ± 0.05 Å, respectively, to R_{Nd-Si} = 3.82 ± 0.03 Å and R_{Nd-Ca} = 3.87 ± 0.03 Å, respectively, over 270 days aging. Thus, the reported distances R_{Nd-Si} and R_{Nd-Ca} are shorter after aging C–S–H for 270 days compared to those determined in the CEMHYD-200-26 cement sample (Table 2). Note that C–S–H phases in HCP are expected to have a C/S ratio in the above range. The coordination numbers were reported to be N_{Si} = 3.7 ± 0.4 and N_{Ca} = 4.9 ± 1.9 in the amorphous C–S–H samples after 270 days aging. The coordination number N_{Si} is lower than in CEMHYD-200-26 while N_{Ca} is similar (within the uncertainties of the measurements). The reason for these differences in the structural parameters (bond-distances, coordination numbers) is presently unclear. A tentative explanation can be given by taking into account differences in the crystallinity of "inner"–C–S–H formed in cement paste and the amorphous C–S–H phases prepared in the laboratory. Note that, in hydrated cement, Nd accumulates in rims around "inner"–C–S–H phases. In situ formation of the latter phases may be much slower than precipitation of synthetic C–S–H phases, thus allowing better crystallized C–S–H phases to be formed in HCP. This conclusion is consistent with observations made by BSE gray scale contrast imaging (18). "Inner"–C–S–H phases have a higher density (in line with the lighter gray tone in BSE imaging) than "outer"–C–S–H phases, which suggest presence of better crystallized material. Thus, it is concluded that the coordination environment of Nd in the denser "inner"–C–S–H and in synthetic C–S–H phases may be different. Further, the coordination environment of Nd in well-crystallized C–S–H phases may be representative for Nd bound in "inner"–C–S–H phases of the cement matrix.

Implications for Radioactive Waste Management. The safe disposal and long-term storage of radioactive waste is a major worldwide concern and a primary environmental task. The capability of near field materials to immobilize radionuclides is an important aspect of safety considerations. Efficiency of immobilization processes has direct consequences on the release of radionuclides from the near field into the far field surrounding a repository for radioactive waste. In this context, the results from the present study provide new evidence for the long-term safe disposal of an important class of radionuclides, i.e., the trivalent actinides such as [241/243]Am. First, it is shown that trivalent lanthanides, and by analogy trivalent actinides, may be preferentially accommodated by C–S–H phases in hydrated cement. The latter results corroborate those of an earlier TRLFS study (6), which showed that Cm(III) preferentially sorbs to C–S–H phases in the cement matrix. This finding, in combination with the observed long-term persistence of C–S–H phases in an evolving cementitious near field (25), implies that the uptake-controlling cement phase for trivalent actinides (i.e., C–S–H phases) could be present in a cement-based repository over long time periods. Second, this study shows that

binding into the structure of C–S–H phases is most likely the dominant mode of Nd immobilization. Again, this finding supports the results of an earlier study (8), which proposed Cm(III) incorporation into the Ca sheets and interlayer of C–S–H phases. Incorporation into the structure further implies that trivalent actinides could be accommodated in C–S–H phases for long time periods. Thus, the binding mechanisms proposed in this study supports the idea of long-term safe disposal of trivalent actinides in cement-based repositories for radioactive waste.

Note Added after ASAP Publication
There was an error in Figure 3 artwork and caption, and reference 23 was modified in the version published ASAP September 9, 2009; the corrected version was published ASAP October 2, 2009.

Supporting Information Available
Table S1 chemical conditions of the Nd cement-sample preparation for the μ-XAS and bulk-XAS measurements; Figure S1 Nd/Ca correlation plot; Figure S2 Nd L_{III}-edge experimental spectra for μ-EXAFS and bulk-EXAFS measurements of selected Nd doped HCP samples with a water/cement ratio of 0.4, varying reaction time (15 min., 1 day, and 28 days), and total metal concentration of 26 μmol/g solid phase, and Nd doped portlandite; further details on the EXAFS data reduction and derivation of the EXAFS model. This material is available free of charge via the Internet at http://pubs.acs.org.

Literature Cited
(1) Chapman, N.; McCombie, C. *Principles and Standards for the Disposal of Long-Lived Radioactive Wastes*; Waste Management Series 3; Elsevier: Amsterdam, 2003.

(2) Shannon, R. Revised effective ionic radii and systematic studies of interatomic distances in halides and chalcogenides. *Acta Crystallogr. A* **1976**, *32* (5), 751–767.

(3) Atkins, M.; Glasser, F. P. Application of Portland cement-based materials to radioactive waste immobilization. *Waste Manage.* **1992**, *12*, 105–131.

(4) Vespa, M.; Dähn, R.; Gallucci, E.; Grolimund, D.; Wieland, E.; Scheidegger, A. M. Micro-scale investigation of Ni uptake by cement using a combination of scanning electron microscopy and synchrotron-based techniques. *Environ. Sci. Technol.* **2006**, *40* (24), 7702–7709.

(5) Vespa, M.; Dähn, R.; Grolimund, D.; Harfouche, M.; Wieland, E.; Scheidegger, A. M. Speciation of heavy metals in cement-stabilized waste forms: A micro-spectroscopic study. *J. Geochem. Explor.* **2006**, *88*, 77–80.

(6) Stumpf, T.; Tits, J.; Walther, C.; Wieland, E.; Fanghänel, T. Uptake of trivalent actinides (curium(III)) by hardened cement paste: a time-resolved laser fluorescence spectroscopy study. *J. Colloid Interface Sci.* **2004**, *276* (1), 118–124.

(7) Schlegel, M. L.; Pointeau, I.; Coreau, N.; Reiller, P. Mechanism of Europium retention by calcium silicate hydrates: An EXAFS study. *Environ. Sci. Technol.* **2004**, *38* (16), 4423–4431.

(8) Tits, J.; Stumpf, T.; Rabung, T.; Wieland, E.; Fanghanel, T. Uptake of Cm(III) and Eu(III) by calcium silicate hydrates: A solution chemistry and time-resolved laser fluorescence spectroscopy study. *Environ. Sci. Technol.* **2003**, *37* (16), 3568–3573.

(9) Vespa, M.; Dähn, R.; Grolimund, D.; Wieland, E.; Scheidegger, A. M. Spectroscopic investigation of Ni speciation in hardened cement paste. *Environ. Sci. Technol.* **2006**, *40* (7), 2275–2282.

(10) Vespa, M.; Dähn, R.; Grolimund, D.; Wieland, E.; Scheidegger, A. M. Co speciation in hardened cement paste: A macro- and micro-spectroscopic anvestigation. *Environ. Sci. Technol.* **2007**, *41* (6), 1902–1908.

(11) Wieland, E.; Tits, J.; Ulrich, A.; Bradbury, M. H. Experimental evidence for solubility limitation of the aqueous Ni(II) concentration and isotopic exchange of Ni-63 in cementitious systems. *Radiochim. Acta* **2006**, *94* (1), 29–36.

(12) Marcus, M. A.; MacDowell, A. A.; Celestre, R.; Manceau, A.; Miller, T.; Padmore, H. A.; Sublett, R. E. Beamline 10.3.2 at ALS: a hard X-ray microprobe for environmental and materials sciences. *J. Synchrotron Radiat.* **2004**, *11* (3), 239–247.

(13) Newville, M. EXAFS analysis using FEFF and FEFFIT. *J. Synchrotron Radiat.* **2001**, *8* (2), 96–100.

(14) Ravel, B.; Newville, M. ATHENA, ARTEMIS, HEPHAESTUS: data analysis for X-ray absorption spectroscopy using IFEFFIT. *J. Synchrotron Radiat.* **2005**, *12*, 537–541.

(15) Bacchi, A.; Lamzin, V. S.; Wilson, K. S. A self-validation technique for protein structure refinement: the extended Hamilton test. *Acta Crystallogr.* **1996**, *D 52* (4), 641–646.

(16) Downward, L.; Booth, C. H.; Lukens, W. W.; Bridges, F. A variation of the F- test for determining statistical relevance of particular parameters in EXAFS fits. *AIP Conference Proc.* **2007**, *882* (1), 129–131.

(17) Hamilton, W. Significance tests on the crystallographic R factor. *Acta Crystallogr.* **1965**, *18* (3), 502–510.

(18) Scrivener, K. L. Backscattered electron imaging of cementitious microstructures: understanding and quantification. *Cem. Concr. Res.* **2004**, *26* (8), 935–945.

(19) Stumpf, S.; Stumpf, T.; Dardenne, K.; Hennig, C.; Foerstendorf, H.; Klenze, R.; Fanghanel, T. Sorption of Am(III) onto 6-line-ferrihydrite and its alteration products: Investigations by EXAFS. *Environ. Sci. Technol.* **2006**, *40* (11), 3522–3528.

(20) Mandaliev, P.; Wieland, E.; Daehn, R.; Tits, J.; Wehrli, B. EXAFS study of Nd (III) binding to amorphous calcium silicate hydrates (C-S-H) J. Colloid Interface Sci. 2008, in press.

(21) Lothenbach, B.; Wieland, E. A thermodynamic approach to the hydration of sulphate-resisting Portland cement. *Waste Manage.* **2006**, *26* (7), 706–719.

(22) Lothenbach, B.; Winnefeld, F. Thermodynamic modelling of the hydration of Portland cement. *Cem. Concr. Res.* **2006**, *36* (2), 209–226.

(23) Mandaliev, P. Mechanisms of Nd(III) and Eu(III) uptake by cementitious materials. Swiss Federal Institute of Technology Zürich (ETH), Diss. ETH Nr. 18095, Zürich, 2008 (http://les. web.psi.ch/IndexphD.html).

(24) Merlino, S.; Bonaccorsi, E.; Armbruster, T. The real structure of tobermorite 11 Å: normal and anomalous forms, OD character and polytypic modifications. *Eur. J. Mineral.* **2001**, *13*, 577–590.

(25) Glasser, F. P. Characterisation of the barrier performance of cements. *Mater. Res. Soc. Symp. Proc.* **2002**, *713*, 721–732.